MNRAS **442,** 1794–1804 (2014) doi:10.1093/mnras/stu891

The main sequence and the fundamental metallicity relation in MaGICC Galaxies: evolution and scatter

A. Obreja,[1★] C. B. Brook,[1] G. Stinson,[2] R. Domínguez-Tenreiro,[1] B. K. Gibson,[3,4] L. Silva[5] and G. L. Granato[5]

[1]*Departamento de Física Teórica, Universidad Autónoma de Madrid, Cantoblanco, E-28049 Madrid, Spain*
[2]*Max-Planck-Institut für Astronomie, Königstuhl 17, D-69117 Heidelberg, Germany*
[3]*Institute for Computational Astrophysics, Dept of Astronomy & Physics, Saint Mary's University, Halifax, NS B3H 3C3, Canada*
[4]*Jeremiah Horrocks Institute, University of Central Lancashire, Preston PR1 2HE, UK*
[5]*Osservatorio Astronomico di Trieste, INAF, Via Tiepolo 11, I-34131 Trieste, Italy*

Accepted 2014 May 2. Received 2014 May 2; in original form 2013 December 16

ABSTRACT

Using cosmological galaxy simulations from the MaGICC project, we study the evolution of the stellar masses, star formation rates and gas-phase abundances of star-forming galaxies. We derive the stellar masses and star formation rates using observational relations based on spectral energy distributions by applying the new radiative transfer code GRASIL-3D to our simulated galaxies. The simulations match well the evolution of the stellar mass–halo mass relation, have a star-forming main sequence that maintains a constant slope out to redshift $z \sim 2$, and populate projections of the stellar mass – star formation – metallicity plane, similar to observed star-forming disc galaxies. We discuss small differences between these projections in observational data and in simulations, and the possible causes for the discrepancies. The light-weighted stellar masses are in good agreement with the simulation values, the differences between the two varying between 0.06 and 0.20 dex. We also find good agreement between the star formation rate tracer and the true (time-averaged) simulation star formation rates. Regardless, if we use mass- or light-weighted quantities, our simulations indicate that bursty star formation cycles can account for the scatter in the star-forming main sequence.

Key words: galaxies: abundances – galaxies: evolution – galaxies: formation – galaxies: star formation – galaxies: stellar content.

1 INTRODUCTION

The manner in which galaxies evolve and grow over their lifetime is reflected in the observed correlation between their star formation rate (SFR) and their assembled stellar mass, dubbed the *main sequence* (MS) *of star formation*. In the Local Universe, the SFRs and stellar masses of star-forming galaxies correlate tightly (e.g. Brinchmann et al. 2004; Elbaz et al. 2007; Noeske et al. 2007), and the relation has also been shown to hold at higher redshifts (Daddi et al. 2007; Bouwens et al. 2011; Karim et al. 2011; Wuyts et al. 2011; Whitaker et al. 2012, among others). The slope of the MS remains relatively constant with redshift, with the zero-point evolving in the sense that high-redshift galaxies form stars at a higher rate than local galaxies of similar stellar mass (Wuyts et al. 2011; Whitaker et al. 2012). The scatter around the MS shows little dependence on mass, or on redshift. There is a hint of increased scatter with decreasing stellar mass (e.g. Whitaker et al. 2012).

Complementary to the locus of star-forming galaxies on the MS, the relation between the mass and metallicity of galaxies provides further insights and constraints on the history and evolution of galaxies. The mass–metallicity (*M–Z*) relation connects stellar masses to both the gas phase (e.g. Garnett 2002; Tremonti et al. 2004) and stellar metallicities (Cowie & Barger 2008; Pérez-Montero et al. 2009), and it has been observed over a range of redshifts (Tremonti et al. 2004; Erb et al. 2006; Kewley & Ellison 2008; Maiolino et al. 2008; Zahid, Kewley & Bresolin 2011; Henry et al. 2013a,b; Lara-López et al. 2013). At all z, the lower mass systems have lower metallicities. We note here that care must be taken in interpreting and reconciling these results, as the evolution of the relation is subject to differences in the observational techniques used at different redshifts and to calibrations of their abundances based on observed rest-frame optical line ratios (e.g. Zahid et al. 2011).

The star-forming MS and mass–metallicity relation have been combined in *the fundamental metallicity relation* (FMR), relating the stellar mass, gas-phase metallicity and the SFR of galaxies (Lara-López et al. 2010; Mannucci et al. 2010). The FMR reflects the cycle of inflows that feed star formation, the production of

★E-mail: aura.obreja@uam.es

metals and enrichment of the interstellar medium (ISM), and the subsequent outflows that are driven by the energy released by the forming stellar populations (see Davé, Finlator & Oppenheimer 2012; Dayal, Ferrara & Dunlop 2013; Hirschmann et al. 2013; Lilly et al. 2013).

These indicators of galaxy formation and growth provide important constraints on galaxy formation models. Perhaps the most ambitious of these models are those that include baryonic physics, employing hydrodynamics to follow the evolution of gas and star formation within a fully cosmological context, and allowing a detailed description of the structural, chemical and dynamical properties within the galaxies (Katz 1992; Steinmetz & Mueller 1994; Katz, Weinberg & Hernquist 1996).

Certainly, significant progress has been made with such models in recent years. In particular, simulations that regulate star formation in order to be more consistent with the empirical relation between stellar mass and halo mass (Guo et al. 2010; Moster et al. 2010) are having success in forming more realistic galaxies (Brook et al. 2011, 2012; Guedes et al. 2011; McCarthy et al. 2012; Aumer et al. 2013; Munshi et al. 2013; Marinacci, Pakmor & Springel 2014). A range of different feedback schemes have been used in these studies, and in particular many augment feedback from supernovae (SNe) with feedback from massive stars prior to their explosion as SNe (Stinson et al. 2013). Suffice to say that the recent simulations all input significantly more energy than was generally used in previous generations, which generally suffered from severe loss of angular momentum (see, however, Sáiz et al. 2001; Doménech-Moral et al. 2012), and too much mass in the central regions (e.g. Navarro & Steinmetz 2000; Piontek & Steinmetz 2011).

High-resolution MaGICC 'zoom' simulations have been shown to match the stellar mass–halo mass relation over a wide range in mass, as well as a variety of scaling relations at $z = 0$, including those between luminosity, rotation velocity, size, H I gas content and metallicity (Brook et al. 2012; Stinson et al. 2013). No scaling with mass for the outflows, no mass-loading or direction of outflows is input by hand in our simulations, so any scaling with galaxy mass arises naturally from the energy feedback implementation. These simulations also have slowly rising rotation curves and appropriately large disc-to-total ratios.

For redshifts $z > 2$, using relatively low-resolution simulations where hydrodynamics was used throughout a volume of 114 Mpc^3, the simulated galaxies have also been shown to match the observed slope and scatter in the stellar mass–halo mass relation and galaxy stellar-mass function for galaxies with stellar mass $M_* > 5 \times 10^{10}\,\mathrm{M}_\odot$ (Kannan et al. 2014).

We now further test our suite of high-resolution 'zoom' MaGICC simulated galaxies by studying their evolution in the parameter space of halo mass, stellar mass, SFR and gas-phase metal abundance, and we discuss our results in comparison with observational data. In what can be considered an accompanying paper (Brook et al. 2013), we have characterized the baryon cycle by quantifying the inflows, outflows and recycling rates of gas and metals into, and out of, the virial radius and star-forming regions of our simulations. The evolution of the properties of stellar mass, SFRs and metallicity that we follow in this paper are a direct reflection of this baryon cycle.

The paper is outlined as follows: in Section 2, we recap the essential features of our simulations. In Section 3, we outline how we post-process our simulations using GRASIL-3D (Domínguez-Tenreiro et al. 2014) and derive stellar masses and SFRs from synthetic spectral energy distributions (SEDs) that include the effects of dust. The evolution of the stellar mass–halo mass relation is shown in Section 4.1, followed by the evolution of the star-forming MS and its scatter in Sections 4.2 and 4.3, respectively. The mass–metallicity relation and the FMR are presented in Sections 4.5 and 4.4. Similarities and differences with observational data are highlighted in each of these sections. Section 5 summarizes our conclusions.

2 THE SIMULATIONS

We analyse eight cosmological zoom simulations from the MaCICC project (Brook et al. 2012; Stinson et al. 2013), run with GASOLINE (Wadsley, Stadel & Quinn 2004), a parallel smoothed particle hydrodynamics (SPH) tree-code. Initial conditions are derived from the McMaster Unbiased Galaxy Simulations (Stinson et al. 2010). The simulations include metal line cooling (Shen, Wadsley & Stinson 2010), the effect of an ultraviolet ionizing background, SN and early stellar feedback. We describe here the most important implementations and refer the reader for details of the code to Wadsley et al. (2004), and of the feedback implementation to Stinson et al. (2010).

Stars are produced with an SFR $\propto \rho^{1.5}$ from cool ($T < 15\,000$ K) and dense ($n_{\mathrm{th}} > 9.3\,\mathrm{cm}^{-3}$) gas, with a star formation efficiency parameter of 0.017. The blastwave formalism (Stinson et al. 2006) is used to implement SN feedback, at the end of massive stars (8 $\mathrm{M}_\odot$) lifetime, 10^{51} erg of energy being deposited into the surrounding medium. Prior to their explosion as SNe, massive stars inject energy into the surrounding gas. This feedback mechanism has also been included (Stinson et al. 2013) as pure thermal energy feedback in order mimic the weak coupling to the surrounding gas (Freyer, Hensler & Yorke 2006). Thermal energy feedback is highly inefficient in these types of simulations (Katz 1992; Kay et al. 2002) due to our inability to resolve the ISM of star-forming regions, with a significant amount of the injected energy radiated away prior to the next simulation timestep, resulting in an inefficient coupling of early stellar feedback to the ISM.

A Chabrier initial mass function (IMF; Chabrier 2003) is used to compute the ejected mass and metals, which are distributed among the nearest neighbour gas particles according to the smoothing kernel (Stinson et al. 2006). Metal abundances are based on the SNII yields of Woosley & Weaver (1995) and SNIa yields of Nomoto et al. (1997). The turbulent metal mixing is mimicked using a shear-dependent diffusion term (Shen et al. 2010). Cooling rates are computed by taking into account the diffused metals.

In Table 1, we give the stellar and virial masses at $z = 0$, the SPH smoothing lengths and the initial mass of gas particles for the simulated galaxies.

Table 1. Simulation data where m_{gas} is the initial mass of gas particles, h_{soft} the minimum SPH smoothing length, and M_{vir} and M_{star} the total and stellar masses within the virial radius (Bryan & Norman 1998) at $z = 0$.

Name	m_{gas} ($10^4\,\mathrm{M}_\odot$)	h_{soft} (pc)	M_{vir} ($10^{10}\,\mathrm{M}_\odot$)	M_{star} ($10^9\,\mathrm{M}_\odot$)
g21647_L*	18.9	312	79.18	25.11
g1536_L*	18.9	312	67.95	23.61
g7124	18.9	312	41.80	6.29
g15784	7.5	156	16.42	4.26
g15807	7.5	156	27.81	1.47
g1536-Irr	7.5	156	7.71	0.45
g5664	7.5	156	5.92	0.24
g21647-Irr	7.5	156	9.18	0.20

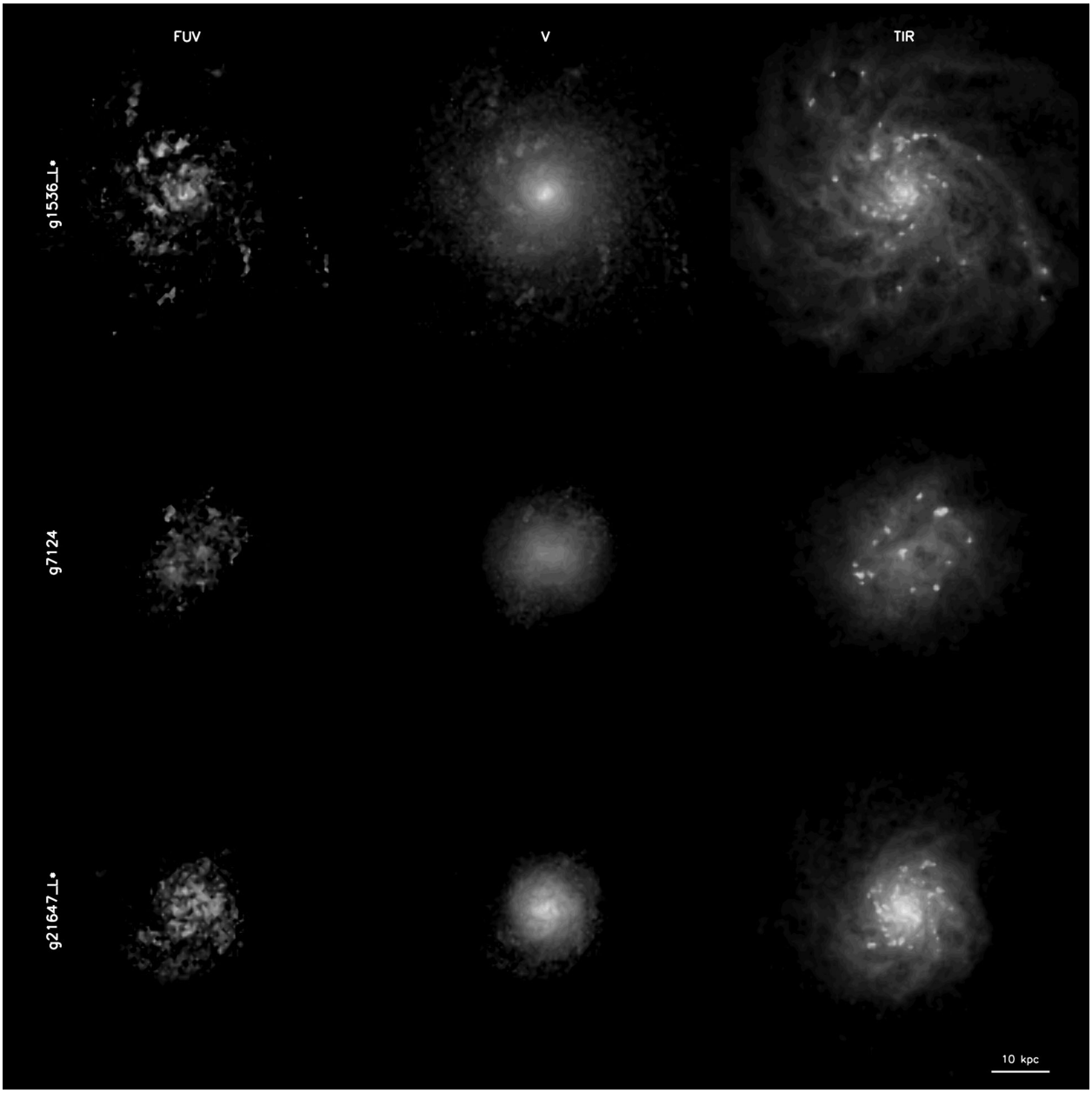

Figure 1. Example of GRASIL-3D images in the spectral ranges of far-UV, visible and total IR (from left to right) for three of the more massive simulated galaxies at $z = 0$.

3 POST-PROCESSING WITH GRASIL-3D

In order to make a more meaningful comparison with observational data, we model the light-weighted quantities for stellar masses and SFRs. For this purpose, we used the radiative transfer code, GRASIL-3D (Domínguez-Tenreiro et al. 2014), which is capable of generating SEDs for simulated galaxies of arbitrary geometries, taking into account the dust processed light from stellar populations. These calculations assumed the same Chabrier IMF as used in the simulations, and the stellar library from Bruzual & Charlot (2003). We use a parameter set that governs the destruction of molecular clouds by the embedded stars which leads to fluxes from visible to IR in the ranges spanned by observational data samples. This parameter set has escape time-scale from molecular clouds of $t_0 = 10$ Myr, radius for the clouds of $r_{\rm mc} = 14$ pc, a cloud threshold density of $\rho_{\rm mc,\,thres} = 3.3 \times 10^9\,{\rm M}_\odot\,{\rm kpc}^{-3}$ and a log-normal probability distribution function (Wada & Norman 2007) with $\sigma = 3.0$, while the mass of a single cloud is assumed to be $m_{\rm mc} = 10^6\,{\rm M}_\odot$.

We construct GRASIL-3D inputs for all the snapshots with $z < 3.5$ of the eight simulated galaxies, and obtained the face-on surface brightness profiles in the r band. We then derive the Petrosian radii, $R_{\rm P}$ (Blanton et al. 2001), which we use to define the radial limits of our simulated galaxies ($R_{\rm lim} = 2R_{\rm P}$). GRASIL-3D calculations have been done in the rest frame of the objects. Luminosities, fluxes and colours have been computed from the integrated face-on SEDs within $R_{\rm lim}$. Therefore, our sample consists in eight galaxies 'observed' at various times in their evolution. In Fig. 1, we show an example of GRASIL-3D images, in relevant bands for this study for three of the more massive simulated galaxies at $z = 0$.

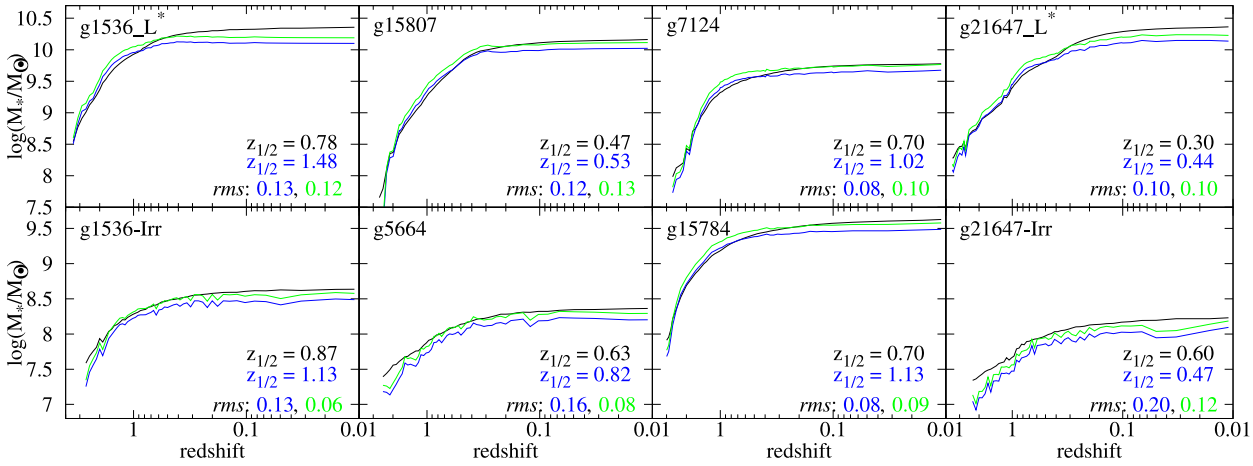

Figure 2. Stellar mass assembly for the simulated galaxies as predicted by simulations (black curves), and as derived using the $B - V$ colours and mass-to-light ratios in the B band (blue curves) and V band (green curves), respectively. The half-mass redshift, $z_{1/2}$ is given in each case for the black and blue curves. The rms scatter of the stellar mass derived using the $B - V$ colours and the mass-to-light ratios in the B and V bands with respect to the *real* mass are also shown.

All post-processing with GRASIL-3D has been done using fixed parameters, which are nevertheless suitable for both starburst and quiescent galaxies (Domínguez-Tenreiro et al. 2014). Also, all observables have been computed in the rest frame of the objects, and no detector properties apart from the transmissions in each band have been taken into account. Since we use broad-band fluxes from far-UV (FUV) to far-IR to estimate stellar masses and SFR, over a wide range of mass, these limitations are important. Technically, at high redshift, our smallest galaxies could not be observed in all bands we employ. Therefore, our comparison of light- and mass-weighted quantities is an idealized one. Nevertheless, the process of viewing the simulations in a manner analogous to observers helps to build confidence in the comparisons we make between observations and simulations.

There are various ways in which intrinsic properties like mass and SFR are inferred from observables. In the case of stellar masses, the current most widely used method is SED fitting, which became feasible with the recent advance in accurate multiwavelength data and the refinement of stellar population synthesis models to include effects like post-MS stellar evolution. We decided to use simple colour-dependent mass-to-light relations, which nevertheless have been tested against other methods, like the Tully–Fisher one. The recent work of McGaugh (in preparation) provides colour-dependent mass-to-light relations in four different bands (B, V, Ks and IRAC 3.6 μm). We use the B- and V-band mass-to-light ratios, which return masses closer to the simulations values than the ones in the Ks and IRAC 3.6 μm bands.

Global SFRs can be inferred using emission lines or broad-band fluxes (see Kennicutt & Evans 2012, for a review on SFR tracers). In our study, we employ the FUV tracer of Hao et al. (2011), where the FUV flux is corrected for dust obscuration using the total IR emission (TIR). These tracers reflect the SFR over timescales of ∼100 Myr, which are well resolved by our simulations. Therefore, mass-weighted SFR are time-averaged over 100 Myr. One thing to keep in mind is that a good estimation of the TIR flux is observationally difficult, especially for dwarf galaxies.

We first checked whether our galaxies fall within the $B - V$ and M_V ranges spanned by the data sample used by McGaugh (in preparation). We also checked the ranges spanned by our objects in the IRX $= \log(L_{\rm TIR}/L_{\rm FUV,obs})$ versus FUV − NUV diagram (fig. 3 of Hao et al. 2011), finding that the majority of our objects have IRX within [0.19, 2.39] and FUV − NUV within [0.07, 1.06], and moreover fall close the curve defined by the observational sample employed by Hao et al. (2011), albeit with a large dispersion (0.46 dex). While the observational sample contains only local normal star-forming galaxies, some of the simulations snapshots correspond to peaks of star formation and some of the objects are dwarfs, cases outside of the sample used for the calibration. The error in the IRX-based attenuation correction for starburst is, in any case, <0.3 mag (Hao et al. 2011). On the other hand, this prescription when applied to dwarfs might suffer from problems. Indeed, the highest rate of discrepancy in the IRX versus FUV − NUV occurs for the two lowest mass simulations (g5664 and g21647-Irr), which have a significant number of snapshots with IRX < 0.19 (35 and 56 per cent, respectively). However, even in these two cases, the synthetic SFR closely follows the real one.

We shall be calling the whole sample *complete*, and the corresponding restriction to the observational ranges of Hao et al. (2011) and McGaugh (in preparation), *limited*. There is no significant difference in our results between these two samples, as can be seen in consistency between the light- and mass-weighted stellar mass and SFR in Figs 2 and 3.

In Fig. 2, we give the stellar mass assembly tracks for the simulated galaxies. The black lines are obtained by summing the stellar mass within $R_{\rm lim}$; the coloured lines are obtained by applying the mass tracers from McGaugh (in preparation), with blue (green) based on the M/L ratio in the B band (V band). The two light-weighted stellar masses follow quite closely the true simulation stellar mass, the difference being no larger than 0.20 dex. Fig. 2 indicates that the most massive galaxies at low redshifts are better traced by the V-band-derived masses, while at higher z the B-based stellar mass gives slightly better results. On the other hand, for the lower mass systems (g1536-Irr, g5664 and g21647-Irr), the V band is a better tracer than the B band at all z. We also give the half-mass redshift for each galaxy. The values of $z_{1/2}$ for the direct simulation tracks are systematically lower than those from the light-processed tracks, with the exception of g21647_L*. The biggest difference between the corresponding half-mass formation times is 2.6 Gyr for g1536_L*, while the smallest one is 0.4 Gyr for g15807. The specific values of half-mass formation times for the simulated galaxies are within the observational constraints of Kauffmann (2014), for example, who studied a subsample of SDSS-DR7. These

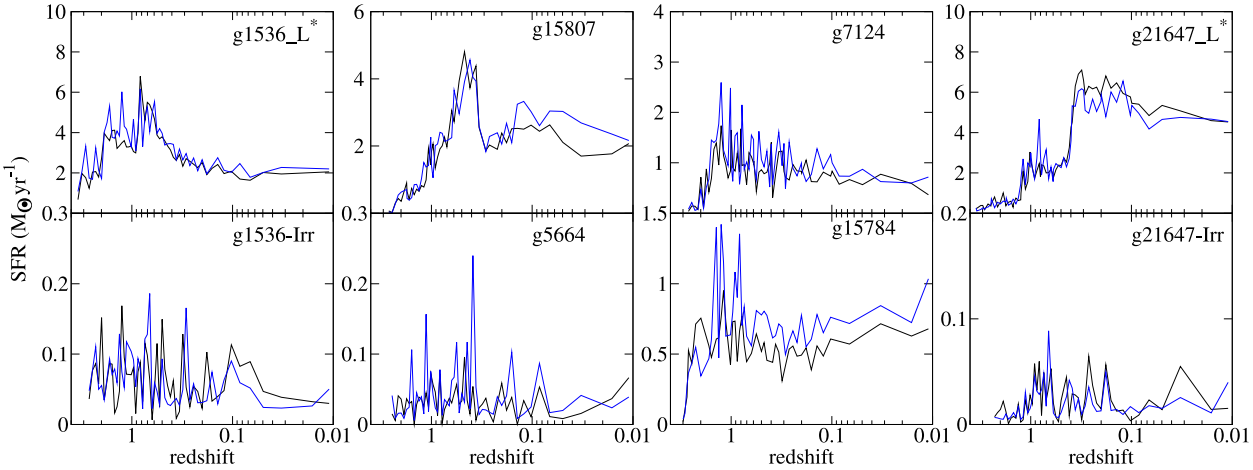

Figure 3. SFR histories for the simulated galaxies as predicted by simulations (black curves), and as derived using the infrared-corrected FUV luminosities (blue curves). The *observational* SFRs are fairly consistent with the *real* ones.

observations, however, are restricted to the central regions of galaxies which contain no more than ∼30 per cent of the total light.

The differences between the light-weighted (blue) and mass-weighted (black) SFRs are shown in Fig. 3, where light-weighted SFRs are derived from IR-corrected FUV luminosities (Hao et al. 2011). This SFR tracer is based on the correlation between the IR/UV luminosity ratio and UV colour, which is used to estimate the dust attenuation. The mass-weighted SFRs were computed by counting all the stellar particles that formed in the last 100 Myr of each simulation snapshot. This time interval for averaging has been used in order to be consistent with the SFR tracer. The observational tracer follows closely the bursty simulation SFR. The differences between the 'observed' and 'true' SFRs are linked to the assumptions used when constructing the tracer. For example, the attenuation-corrected FUV luminosities of Hao et al. (2011) are consistent with evolutionary synthesis models which assume a constant solar metallicity.

The mean fraction of SFR coming out in IR (averaging over all the snapshots of a simulated galaxy) increases linearly with $\log(M_*)$ at $z = 0$. At the low-mass end ($M_* \sim 10^8$ M$_\odot$), the IR flux contributes 25 per cent to the global SFR, increasing to 80 per cent of the total SFR for $M_* \sim 10^{10}$ M$_\odot$. For the three most massive galaxies (g1536_L*, g15807 and g21647_L*), this fraction increases quite smoothly with decreasing z, while for the less-massive galaxies it is highly variable.

Computing light-weighted quantities from face-on images means we are minimizing the effect of dust obscuration. Therefore, we checked the ranges of our observables when different inclinations are considered (face-on to edge-on). For g7124, g1536-Irr, g5664, g15784 and g21647-Irr, the derived mass from edge-on images is $\lesssim$15 per cent less than the face-on values. For the massive galaxies g1536_L* and g15807, the mass decrease can be as high as 25 per cent. g21647_L* has the most extreme inclination effect, with differences between edge-on and face-on up to 50 per cent, although this only occurs at low redshift, $z < 0.4$. For larger redshifts, the effect of inclination for the three massive galaxies is typically ∼20 per cent.

The SFR tracer is less affected by inclination than the mass tracers: typical values of the decrease in derived SFR due to inclination are ∼10 per cent. The effects are slightly lower at higher redshift, and show no clear trend with mass.

4 RESULTS

The effect of different star formation and feedback parameters and implementations applied to a single Milky Way-like galaxy, g1536_L*, has been studied by Stinson et al. (2013). The variation found in the evolution of star formation pointed to the need for feedback from massive stars prior to their explosion as SNe. Using the same feedback scheme, a large sample of high-mass simulated galaxies was also shown to match the relation at high redshift (Kannan et al. 2014). Here, we test the effectiveness of the implemented feedback by exploring the evolution of our suite of high-resolution zoom simulations that span a wide range in stellar mass.

4.1 Evolution of the stellar mass–halo mass relation

In Fig. 4, we show the stellar mass–halo mass relation of our simulated galaxies over plotted on the empirical results from Moster et al. (2013), along with their 1σ scatter, at four redshifts. The galaxies follow the same evolutionary path of stellar mass assembly as those inferred by the abundance matching techniques used in Moster et al. (2013). The stellar masses in this figure are those computed directly from the simulations, but as seen above there is little difference if light-weighted stellar masses are used.

Our suite of simulated galaxies that include early stellar feedback from massive stars, as well as feedback from SNe, not only resemble observations in the Local Universe, but also have stellar masses that evolve with redshift in a manner that resembles real galaxies.

4.2 Evolution of the M_*–SFR relation

The correlation between stellar mass and SFR in galaxies across the cosmic time provides a powerful constraint on the star formation implementations used in simulations. This correlation reflects the mass build-up of galaxies and their morphological diversity. Observationally, the star-forming galaxies have been shown to cluster along the so-called *star formation MS* (Brinchmann et al. 2004; Daddi et al. 2007; Elbaz et al. 2007; Noeske et al. 2007; Bouwens et al. 2011; Karim et al. 2011; Wuyts et al. 2011; Whitaker et al. 2012, among others). This sequence is usually parametrized with a power law (SFR $= \alpha M_*^{\beta}$), where both α and β can be taken to vary with the redshift. Typical values of the slope range from ∼0.4 to 1

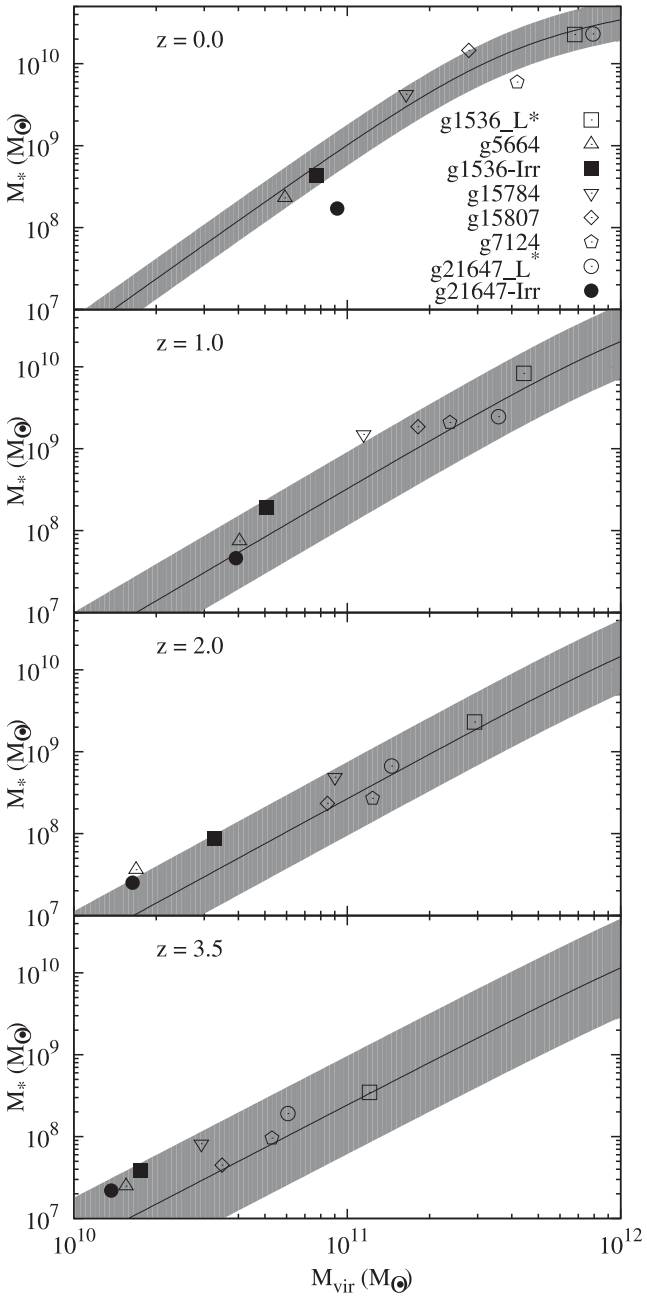

Figure 4. Stellar mass versus halo mass for the simulated galaxies, at four redshifts. The black curves are the abundance matching functions derived by Moster, Naab & White (2013), with their corresponding 1σ deviations (grey areas).

(e.g. Karim et al. 2011; Wuyts et al. 2011; Whitaker et al. 2012; Zahid et al. 2012).

Some studies indicate that the slope remains constant, while the zero-point varies with redshift. For example, Zahid et al. (2012) found that a constant slope $\beta = 0.7$ with $\alpha \sim \exp(1.33z)$ reproduces the observational data up to $z \sim 2.2$. Based on one of the largest mass-complete sample of galaxies up to $z = 2.5$, Whitaker et al. (2012) conclude that the slope of the MS does vary with z, but much less than the normalization. Most relevant to this present study of simulated star-forming galaxies, they find a difference when restricting the sample to the blue star-forming galaxies, for which they find that the slope is approximately 1. Similarly, Wuyts et al. (2011) use a large multiwavelength data set, based on FIREWORKS (Wuyts et al. 2008), and find that a unitary slope reproduces well the observations of (star-forming) disc galaxies, where such galaxies are selected as those having low ($n<2$) Sérsic indices. When fitting a slope of 1, they find that the rms scatter of the MS is only slightly larger than when both slope and normalizations are left to vary.

Studying the tightness of the MS, Salmi et al. (2012) also found an intrinsic slope close to unity, taking into account the effects of mass measurement errors, larger ranges for the SFR at fixed stellar mass and sample completeness. Recent studies have proven that large variations in the MS slope are, to a great extent, an effect of sample selection (Salmi et al. 2012; Whitaker et al. 2012; Guo, Zheng & Fu 2013).

In Fig. 5, we show SFR as a function of stellar mass for three redshift ranges in the simulated galaxies. The upper panels give these quantities as derived directly from the simulations (total stellar mass within $R_{\rm lim}$ and SFR computed with the stellar particles in the same region that formed in a time range of 100 Myr). The lower panels show the SFR based on the tracer of Hao et al. (2011) versus M_*, calculated using the M/L ratios in the B band. The blue points represent only the data that fall within the observational ranges of both Hao et al. (2011) and McGaugh (in preparation), while the cyan ones give the whole simulation sample. The blue and cyan lines are the linear regressions through the corresponding data points. When letting both parameters of the MS vary, we obtain slopes in the range 1.0–1.1. In the plot, we fixed the slope to 1, and explore the scatter. The MS scatter in this case (the rms values shown in each panel) is very similar to the one obtained when both slope and normalization are free. In all panels, simulation data have been superimposed on the data of Wuyts et al. (2011, fig. 1 of their paper).

As shown in Fig. 2, there are small differences between the mass derived using a tracer based on the SED and the real stellar mass. Also the light-weighted SFR (blue curves in Fig. 3) slightly overestimates the 'true' SFR at higher z, the effect being larger for the least massive systems. This translates into a smaller dispersion of SFR at fixed M, as can be seen in Fig. 5 by comparing the lower with the upper panels. As a consequence, the MS scatter is slightly smaller in the 'observed' trends than the 'true' simulation values.

Comparing SFR versus M_* with the observations of Wuyts et al. (2011, fig. 1 of their paper), we see that at low redshift ($z < 0.50$) simulated galaxies populate an MS very close to the extrapolation of the observational sequence. However, at higher redshift the SFRs of simulated galaxies are *below* the extrapolations of the observational relations by ∼0.4–0.5 dex. It is important to keep in mind that observational samples are only complete at high stellar masses (e.g. $M_* > 10^{9.7}$ M$_\odot$). If we compare the ranges spanned by the simulations with their data set, we see that the simulations fall well within the range occupied by observed disc galaxies with Sérsic indices $n < 2.0$ (bottom panels of Fig. 5). Our simulations indicate that low-mass star-forming galaxies should lie below a simple extrapolation of the relation as derived from high-mass galaxies at high redshift. On the other hand, if we compare our data with the MS derived by Guo et al. (2013) in the redshift range 0.6–0.8, the relation in simulations for $0.5 < z < 1.5$ is ∼0.5 dex *above* the observational one.

Due to their shallow potential well, low-mass galaxies are affected to a greater extent by stellar winds, and have burstier star formation histories. However, detection of such systems is not trivial beyond the Local Universe. Recently, Henry et al. (2013a,b) presented a sample of 18 galaxies with stellar masses $M_* < 10^9$ M$_\odot$ at intermediate redshift (z ∼0.6–0.7), with reliably measured emission line fluxes allowing determination of stellar masses and

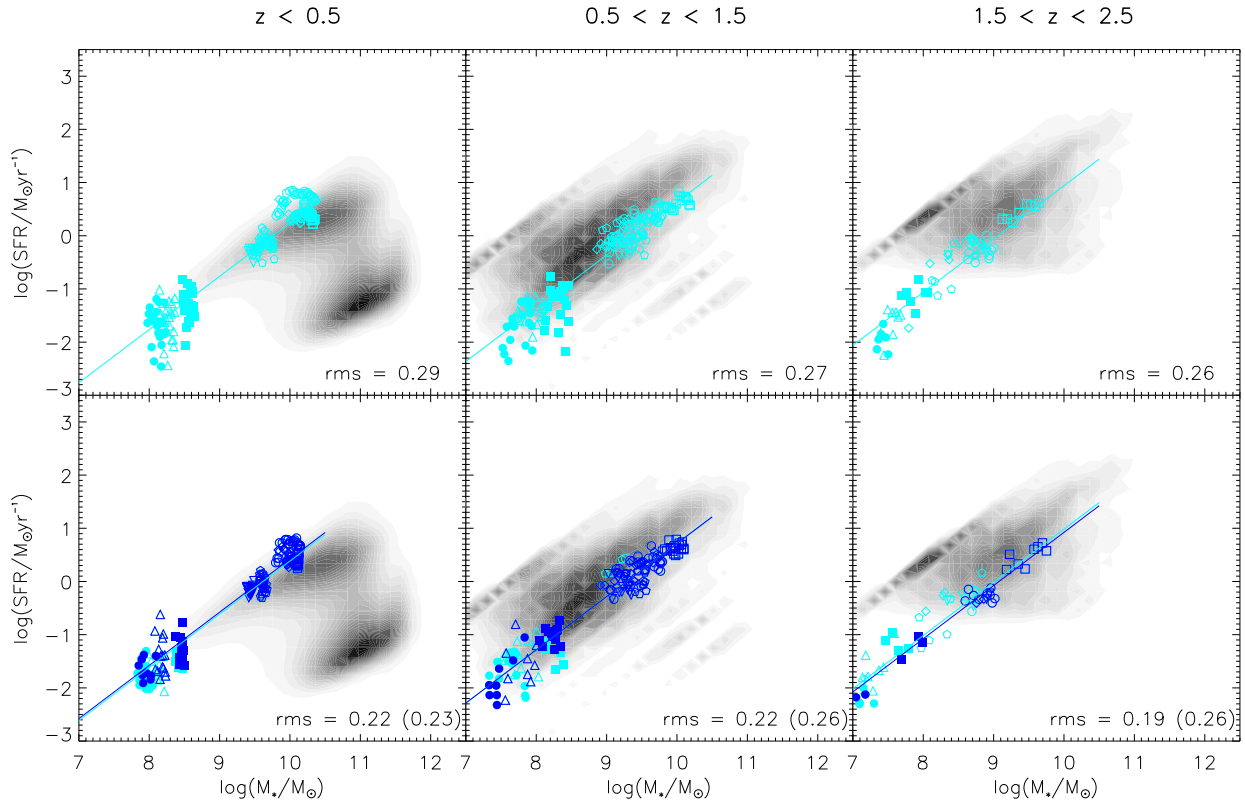

Figure 5. The evolution of M_*– SFR. Top panels: SFR and M_* values are derived from simulations directly. Bottom panels: stellar masses were computed using *B*-band mass-to-light ratios, and the SFR using the TIR-corrected FUV luminosities. Cyan points correspond to the *complete* sample, while blue points represent the *limited* one, including only simulations with observational properties within the ranges used to define the stellar mass and SFR tracers (Hao et al. 2011; McGaugh in preparation). The shape coding is the same as in Fig. 4. The lines are linear fits of constant slope 1 which minimize the scatter. The dispersions around each line are also shown in each corresponding panel. In the bottom panels, the two values of dispersion correspond to the *limited* and *complete* samples, respectively. The grey-scale contours beneath the simulation data are the normalized 2D histograms of the observational sample of Wuyts et al. (2011). In the lowest redshift bin (left-hand panels) the upper overdensity, along which our simulations fall, corresponds to the locus of star-forming galaxies having low Sérsic indices (see fig. 1 of Wuyts et al. 2011).

SFRs from SED fitting. Most of these galaxies have slightly higher SFR values than our simulations, and a scatter with respect to the linear regression (blue line) in the bottom central panel of Fig. 5 of 0.6 dex. Recently, Amorín et al. (2014) presented a sample of star-forming dwarfs up to $z \sim 0.9$, reaching stellar masses as low as 10^7 $M_\odot$. As in the Henry et al. (2013a), these galaxies have slightly higher SFR than our simulations. It is not yet clear whether the higher observed SFRs of this sample is simply a result of the bias towards observing galaxies with high SFRs.

At even higher redshifts, the only available detection method is galaxy lensing (Richard et al. 2011; Christensen et al. 2012; Wuyts et al. 2012; Belli et al. 2013) allowing the observation of distant low mass, relatively low SFR galaxies. These lensed galaxies at $z > 1.5$ have systematically higher SFR than our simulations, typically an order of magnitude higher, but again it is not clear whether there is a selection bias occurring, given the small number of such observed systems.

4.3 Scatter in the M_*–SFR relation

The evolution of the star formation MS strongly constrains galaxy mass assembly. However, it is not only the relation in itself that is important, but also its scatter which reflects the intrinsic variability in the SFR of the star-forming galaxy population.

The SFR history is anything but smooth, the variability increasing with decreasing stellar mass and increasing redshift (see Fig. 3). The high SFR variability of the lower mass systems is a direct consequence of the shallow potential well of these objects: SNe can eject large quantities of gas from the galaxies, with star formation cyclically quenched due to the depletion of the cold gas reservoir (Stinson et al. 2007). As the mass of simulated galaxies increases, the triggering and quenching of star formation due to gas outflows becomes less pronounced.

An advantage of our method of rescaling initial conditions is that we can compare galaxies with different mass that have the same accretion history. Even though they share the same accretion history, it can be seen that g1536-Irr has a significantly more bursty star formation history than g1536_L*, particularly at later times when the potential well of g1536_L* is deeper, but also coupled to the lower gas fraction as the more massive galaxy has been more efficient at converting its gas into stars, as is evident in Fig. 4.

We do not have enough simulated galaxies to derive a statistically robust scatter in the M_*–SFR relation at a given redshift. However, we can test how much scatter comes from the variation in SFR of individual galaxies, as they undergo bursts of star formation and relatively quiescent periods in their evolution. In order to derive such scatter, we have to include data from different time steps within the same z bin, meaning that we must be mindful that the scatter that we measure is not simply the result of the evolution of the relation itself.

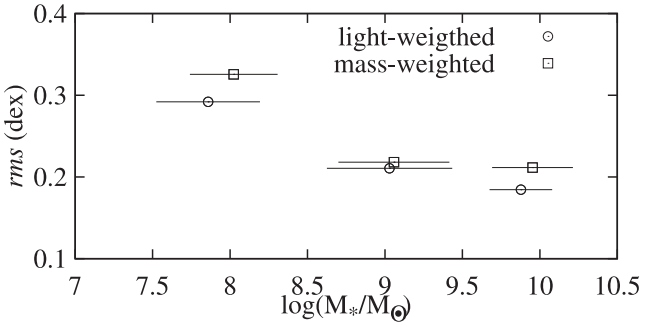

Figure 6. The scatter of the M_*–SFR relation for the simulated galaxies. The x-error bars represent the stellar mass dispersions. Open squares and circles correspond to the mass-weighted sample (cyan points in the top panels of Fig. 5) and to the light-weighted one (cyan points in the bottom panels of the same figure). Since the scatter values have been computed taking into account the evolution of the MS zero-point, the data has not been binned in redshift. For the two samples, a clear trend of decreasing scatter with increasing mass can be appreciated.

The regular evolution of the relation (the zero-point varies linearly with the expansion factor) allows us to find an expected SFR at any z for a given mass, and this can be used to derive the scatter in the MS. In Fig. 6, we show the scatter derived using the expected SFR, as explained above, using the mass- and light-weighted stellar masses and SFRs (open squares and open circles) plotted in the top and bottom panels of Fig. 5, respectively. In order to get an estimate of the scatter variation with mass, we divided the two samples into three equally populated stellar mass bins.

We are able to compute the scatter irrespective of redshift precisely because the reference values for SFR are computed by interpolating the MSs in the three redshift bins. A clear trend of the MS scatter with stellar mass can be appreciated, less-massive galaxies having a higher SFR variability. There is a difference between the scatter computed directly from the simulation outputs (mass-weighted M_* and SFR) and from the 'observed' fluxes (light-weighted M_* and SFR). This difference was expected in light of Fig. 3, where we saw that the SFR tracer better follows the *true* simulation values at high stellar masses than at the low end.

For the light-weighted sample, the scatter goes from ∼0.30 dex for $M_* < 10^8$ M$_\odot$ to ∼0.20 dex for $M_* > 10^9$ M$_\odot$. For the more massive simulated galaxies which have M_* in the range where observational samples are complete, the scatter of $\lesssim$0.3 is similar to the one found by observers (e.g. Daddi et al. 2007; Elbaz et al. 2007; Noeske et al. 2007; Zahid et al. 2012). Therefore, from our small sample of simulated galaxies, it appears that most and perhaps all of the dispersion in the MS could be explained by the intrinsic scatter in the SFR, which is a direct consequence of the bursty star formation history of individual galaxies.

4.4 The mass–metallicity relation

Star formation is primarily governed by the cold gas reservoir available. The stellar mass of galaxies correlates with gas metallicity (Lequeux et al. 1979). While the stellar mass reflects the baryon mass locked into stars, the gas metallicity traces the material reprocessed by stars and the coupling of the galaxy to its environment, in terms of inflows of fresh or pre-enriched gas and the outflows of metals in galactic winds. This correlation provides one of the means by which the feedback processes affecting this baryon cycle can be tested against observations (Brooks et al. 2007).

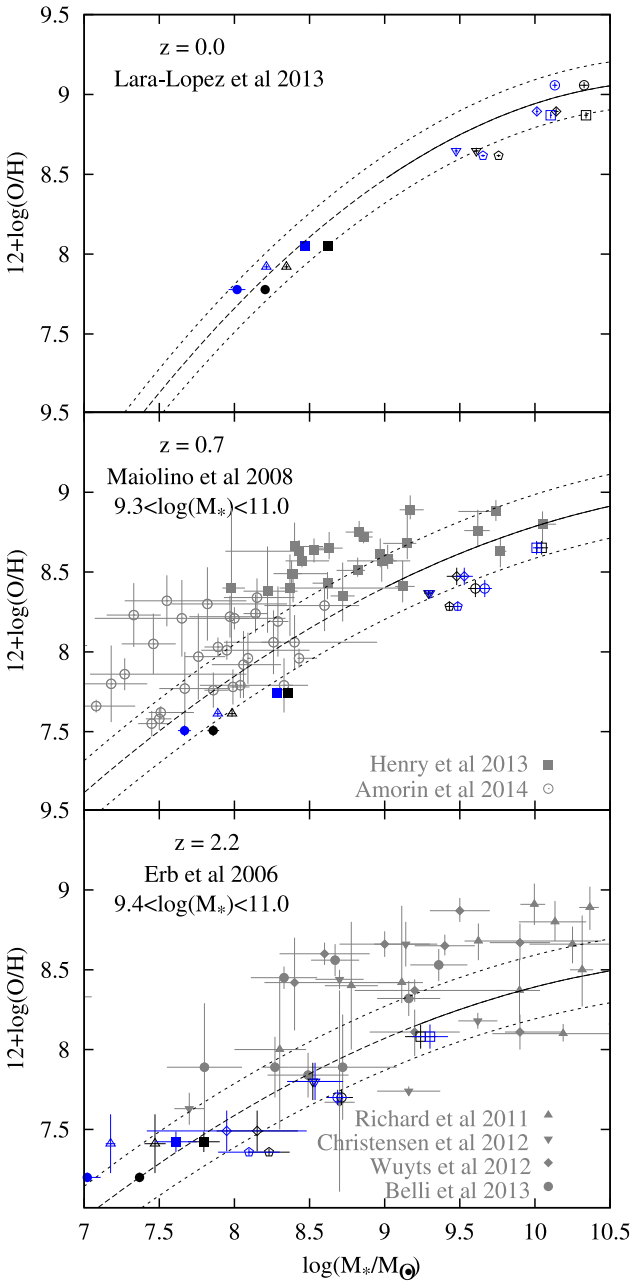

Figure 7. Oxygen abundance as function of stellar mass at three different redshifts. The blue and black points correspond to masses derived using the mass-to-light ratio in the B band and to *true* simulation values, respectively. The shape coding is the same as in Fig. 4. In the centre and bottom panels, we overplotted in grey some of the observational samples (indicated in the corresponding legends) which have the lowest mass system detected at intermediate and high-z. The black solid curves are the observational M–Z relations obtained by Lara-López et al. (2013, top panel), Maiolino et al. (2008, centre panel) and Erb et al. (2006, bottom panel). The dashed black lines give the low-mass extrapolation of these relations, while the dotted black ones give the scatter of 0.15, 0.20 and 0.20 dex, respectively. The limits in the centre and bottom panels indicate the corresponding stellar mass ranges for the samples of Maiolino et al. (2008) and Erb et al. (2006).

In Fig. 7, we show the oxygen abundance versus M_* at three redshifts, chosen to make a comparison with the observational samples in Erb et al. (2006), Maiolino et al. (2008) and Lara-López et al. (2013) at high-, intermediate- and low-z, respectively. The M–Z

relation of Maiolino et al. (2008) has been rescaled to a Chabrier IMF. We use the mean[1] $12 + \log(\mathrm{O/H})$ of the cold gas ($T < 10^4$ K) within $R_{\rm lim}$.

The simulated galaxies follow well these observations at high and low redshift (top and bottom panels), being roughly within the observed scatter from the extrapolations of the *M–Z* relations (Erb et al. 2006; Lara-López et al. 2013). For the $z = 0$, we use the scatter from Lara-López et al. (2013), while for Maiolino et al. (2008) and Erb et al. (2006) curves we assumed a value 0.20 dex. At intermediate z, there is less agreement in absolute values of simulations and the observations of Maiolino et al. (2008), with the former being ∼0.2 dex smaller than the latter in the entire mass range. Yet the trend of metallicity with mass is well reproduced by the simulations even at this intermediate mass range. In simulations, the metallicity evolution between $z \sim 2.2$ and 0.7 varies from ∼0.25 dex for the lowest mass systems up to ∼0.50 dex for the massive ones. A similar trend can be appreciated in observations by comparing the extrapolations of the relations in Erb et al. (2006) and Maiolino et al. (2008). Thus, the difference in metallicity given by the two curves grows from 0.2 dex for $M_* \sim 10^{7.5}$ M$_\odot$ to 0.5 dex for $M_* \sim 10^{9.5}$ M$_\odot$. On the other hand, the observational local *M–Z* relation is steeper than the intermediate and high-z ones, when considering the extrapolation at lower stellar masses.

In the same figure, we over plotted the data from some recent observations which reach stellar masses as low as $M_* \sim 10^{7.6}$ M$_\odot$ at high redshift (Richard et al. 2011; Christensen et al. 2012; Wuyts et al. 2012; Belli et al. 2013). We also show the samples of Henry et al. (2013a) at $z \sim 0.65$ and of Amorín et al. (2014) at $z \lesssim 0.9$. These recent observational high-z samples have larger errors, and generally higher abundances (∼0.2 dex) than the Erb et al. (2006) data. The three most massive simulated galaxies overlap in the *M–Z* plane with these observations. The less massive simulated galaxies, on the other hand, have smaller metallicities than the Richard et al. (2011), Wuyts et al. (2012), Christensen et al. (2012), Belli et al. (2013) samples and show up within 2σ from the extrapolation of Erb et al. (2006) relation. At intermediate redshifts, there is a partial overlap between the Maiolino et al. (2008) observations and the more recent ones by Henry et al. (2013a) and Amorín et al. (2014), although the latter show an offset to higher metallicities with respect to the former. Similar to the high-z, the simulations generally have lower metallicities than these observations.

It is important to note that different methods are used to measure the metallicities in the different studies, meaning that the absolute values are subject to having different calibrations (e.g. Zahid et al. 2012), with different metallicities calibrations resulting in abundances that can vary as much as ∼0.35 dex. We also note that the shape of the *M–Z* relation remains a matter of debate.

4.5 The mass–SFR–metallicity relation

The correlations found between the stellar mass and SFR (Brinchmann et al. 2004) on one hand, and stellar mass and gas metallicity (Lequeux et al. 1979), on the other, raised the question whether they are not just projections of a fundamental relation. In this respect, Ellison et al. (2008) found that indeed the mass–metallicity relation depends on the SFR. Consequently, in two parallel studies, Mannucci et al. (2010) and Lara-López et al. (2010) proposed combinations of these observables (stellar mass, SFR and metallicity) which hold across a wide redshift range (up to $z \sim 3.5$). In the Local Universe, where the gas content of galaxies can be reliably mapped, different combinations of parameters have been probed for correlations. For example, Bothwell et al. (2013) found that the local *M–Z* relation depends on the H I gas mass, and consequently, they were able to construct an FMR with M_*, $M_{\rm H\,I}$ and the gas metallicity. Since we do not have enough statistics in a narrow redshift bin and we are interested in comparing our simulations to observations at high-z, we restrict for now to the M_*–SFR–*Z* correlation.

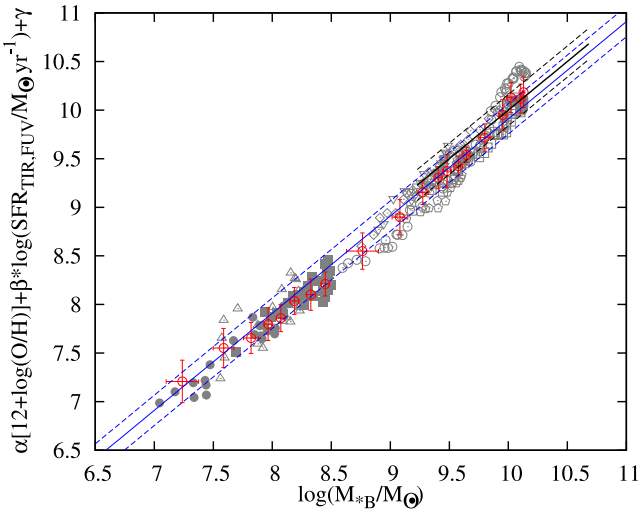

Figure 8. The FMR of star-forming galaxies. The stellar mass is given as a linear combination of $12 + \log(\mathrm{O/H})$ and log(SFR), following Lara-López et al. (2010), with $\alpha = 1.122$, $\beta = 0.474$ and $\gamma = -0.097$. The grey points are the simulated galaxies in the redshift range $z < 3.5$, plotted with the same symbols as in Fig. 4. The solid blue line is the linear fit of constant slope 1 which minimize the scatter, while the dashed blue lines give the corresponding 1σ of 0.16 dex. The open red circles represent the simulations in equally populated stellar mass bins. The solid and dashed black lines are the one to one correspondence of Lara-López et al. (2010) and its 1σ deviation (0.16 dex). The solid blue line is 0.09 dex below the solid black one.

In order to minimize the scatter of the so-called FMR, Mannucci et al. (2010) introduced a new variable, $\mu_\alpha = \log(M_*) - \alpha * \log(\mathrm{SFR})$. A value of $\alpha = 0.32$ minimizes the scatter of median metallicities of SDSS galaxies, while high-z galaxies show the same range of $\mu_{0.32}$ as low-redshift galaxies. In an equivalent way, Lara-López et al. (2010) found that using a linear combination of $12 + \log(\mathrm{O/H})$ and log(SFR), the stellar mass can be recovered with an accuracy of 0.2 dex. Therefore, they proposed that $\log(M_*/\mathrm{M}_\odot) = \alpha[12 + \log(\mathrm{O/H})] + \beta\log(\mathrm{SFR}/\mathrm{M}_\odot\ \mathrm{yr}^{-1}) + \gamma$ with a standard deviation of 0.16 dex, if no errors are considered in metallicity and SFR. They showed that it holds up to redshift ∼3.5.

In Fig. 8, we give the FMR of our simulated galaxies showing a total of 324 snapshots of our suite of simulations between $z = 3.5$ and 0 (grey points), and find that they lie on a linear sequence. We fitted a line through the points allowing both normalization and slope to vary obtaining a scatter only 0.01 dex smaller than when fixing the slope to 1. Thus, we show in solid blue, the FMR obtained by setting the slope to 1 and leaving the zero-point as the only free parameter. The dashed blue line is the corresponding 1σ scatter of 0.16 dex. The FMR of simulated galaxies is ∼0.1 dex below the extrapolation of the observational relation to low-mass and low-metallicity galaxies (solid black line, Lara-López et al. 2010). Within the mass range where the simulations overlap with the Lara-López et al. (2010) sample, the simulations fall within the 1σ scatter of the observations.

[1] Using the median had minimal impact on the results.

While both metallicity and SFR correlate tightly with stellar mass, they correlate loosely, with each other, in simulations and observations alike. In simulations, stellar mass and cold gas metallicity evolve smoothly and in a quite similar manner with redshift, leading to a small scatter in the M–Z relation, while the SFR shows large variations, especially for less massive systems. On the other hand, the metallicity appears to correlate with the specific SFR, but with dwarfs evolving differently than massive galaxies. However, combining the three in the FMR, no redshift evolution is observed and the scatter is reduced with respect to the M_*–SFR relation. The emergence of this plane in the space of M_*–SFR–Z is partially explained by the fact that metallicity increases with decreasing z, while the SFR shows the opposite behaviour. Therefore, to some degree, the redshift dependences of metallicity and SFR compensate each other. We stress, though, that the large dynamical range in this study is obtained by combining snapshots of a small number of galaxies 'observed' at different redshifts. From this perspective, the simulated galaxies evolve along the FMR.

5 CONCLUSIONS

Using cosmological galaxy simulations from the MaGICC project, we study the evolution of the stellar masses, SFRs and gas-phase abundances of star-forming galaxies. We derive the stellar masses and SFRs using observational relations based on SEDs by applying the new radiative transfer code GRASIL-3D to our simulated galaxies.

We compare light-weighted masses and SFRs with the their mass-weighted counterparts from simulations. We find that the simple stellar mass tracers from McGaugh (in preparation), based on integrated colours and mass-to-light ratios are in good agreement with the simulation values, the difference between them being less than ∼0.20 dex. Also, the Hao et al. (2011) SFR tracer based on IR-corrected FUV luminosity follows closely the simulation.

Although the MaGICC simulations have the stellar feedback fixed in order to match the stellar mass–halo mass relation at a given mass and at $z = 0$, all our eight galaxies, spanning two orders of magnitude in mass, actually are within 1σ of the abundance matching curves up to redshift $z \sim 3.5$.

We show that the simulated galaxies populate projections of the stellar mass–SFR–metallicity plane, similar to observed star-forming disc galaxies. Thus, in the $\log(M_*)-\log(\mathrm{SFR})$ plane, simulated galaxies fall along a line of slope 1, up to redshift 2.5, the normalization increasing with z. Both the slope as well as the scatter around these relations are in agreement with observational data. However, the normalizations for the simulated galaxies at higher z are lower than in observations by as much as ∼0.5 dex. This may be a problem for the simulations, yet we emphasize that the simulations are generally of lower mass than complete galaxy surveys, albeit with overlap. A close comparison with Wuyts et al. (2011) data shows that our suite of simulations fall well within the range of observed data. Indeed, there is a hint that the low-mass end of observed data has a lower normalization than the high-mass end. It will be intriguing to see whether this prediction of our model matches future observational samples that are able to probe to lower stellar masses. On our end, a larger sample of simulated galaxies will also allow a more comprehensive comparison of our theoretical model with observations.

Similar to observations, the scatter in the MS seems to be independent of z, and decreasing with increasing stellar mass. By analysing this sample of eight galaxies, 'observed' at different times, we conclude that most of the MS scatter can be explained by the intrinsically bursty history of star formation.

In the stellar mass–gas-phase abundance plane, the simulated discs follow the observations roughly within 2σ up to redshift $z \sim 2.2$. Finally, our sample of simulated star-forming galaxies also show a tight correlation among stellar mass, SFR and metallicity, with the same coefficients as in Lara-López et al. (2010) apart from a difference of 0.09 dex in normalization. The scatter around this FMR is the same as in the observational sample (0.16 dex). The fact that the FMR does not evolve with redshift for our small sample of simulated galaxies, 'observed' over a wide range of z (<3.5), shows that our galaxies grow in away such that the metallicity and SFR evolve in a manner that 'conspires' to maintain the same relation between M_*–Z–SFR. The fact that observed galaxies also evolve in a similarly conspiratorial manner provides support for the baryon cycle within our model. The manner in which the M_*–Z relation depends on SFR at any given redshift will be examined in a future study, using a larger sample of simulated galaxies which will allow galaxies of similar mass to be compared at a given redshift.

ACKNOWLEDGEMENTS

We would like to thank Stijn Wuyts for providing the observational FIREWORKS data used in Fig. 5 and to Arjen van der Wel for useful conversations. We would also like to thank the anonymous referee for the insightful comments and suggestions which have helped to improve the quality of this paper. This work was partially supported by the MICINN and MINECO (Spain) through the grants AYA2009-12792-C03-02 and AYA2012-31101 from the PNAyA, as well as by the regional Madrid V PRICIT programme through the ASTROMADRID network (CAM S2009/ESP-1496) and the 'Supercomputación y e-Ciencia' Consolider-Ingenio CSD2007-0050 project. We also gratefully acknowledge the computer resources provided by BSC/RES (Spain), the Centro de Computación Científica (UAM, Spain), STFCs DiRAC Facility (through the COSMOS: Galactic Archaeology programme), the DEISA Consortium, co-funded through EU FP6 project RI-031513 and the FP7 project RI-222919 (through the DEISA Extreme Computing Initiative), the PRACE-2IP Project (FP7 RI-283493), and the University of Central Lancashire's High Performance Computing Facility. AO is supported by MICINN and MINECO (Spain) through an FPI fellowship. CB thanks MINECO for financial support through contract associated to AYA2009-12792-C03-03 grant. GS received funding from the European Research Council under the European Union's Seventh Framework Programme (FP 7) ERC Grant Agreement no. 321035.

REFERENCES

Amorín R. et al., 2014, preprint (arXiv:1403.3692)
Aumer M., White S., Naab T., Scannapieco C., 2013, MNRAS, 434, 3142
Belli S., Jones T., Ellis R. S., Richard J., 2013, ApJ, 772, 141
Blanton M. R. et al., 2001, AJ, 121, 2358
Bothwell M. S., Maiolino R., Kennicutt R., Cresci G., Mannucci F., Marconi A., Cicone C., 2013, MNRAS, 433, 1425
Bouwens R. J. et al., 2011, ApJ, 737, 90
Brinchmann J., Charlot S., White S. D. M., Tremonti C., Kauffmann G., Heckman T., Brinkmann J., 2004, MNRAS, 351, 1151
Brook C. B. et al., 2011, MNRAS, 415, 1051
Brook C. B., Stinson G., Gibson B. K., Wadsley J., Quinn T., 2012, MNRAS, 424, 1275
Brook C. B., Stinson G., Gibson B. K., Shen S., Macciò A. V., Wadsley J., Quinn T., 2013, preprint (arXiv:1306.5766)
Brooks A. M., Governato F., Booth C. M., Willman B., Gardner J. P., Wadsley J., Stinson G., Quinn T., 2007, ApJ, 655, L17

Bruzual G., Charlot S., 2003, MNRAS, 344, 1000
Bryan G. L., Norman M. L., 1998, ApJ, 495, 80
Chabrier G., 2003, PASP, 115, 763
Christensen L. et al., 2012, MNRAS, 427, 1953
Cowie L. L., Barger A. J., 2008, ApJ, 686, 72
Daddi E. et al., 2007, ApJ, 670, 156
Davé R., Finlator K., Oppenheimer B. D., 2012, MNRAS, 421, 98
Dayal P., Ferrara A., Dunlop J. S., 2013, MNRAS, 430, 2891
Doménech-Moral M., Martínez-Serrano F. J., Domínguez-Tenreiro R., Serna A., 2012, MNRAS, 421, 2510
Domínguez-Tenreiro R., Obreja A., Granato G. L., Schurer A., Alpresa P., Silva L., Brook C. B., Serna A., 2014, MNRAS, 439, 3868
Elbaz D. et al., 2007, A&A, 468, 33
Ellison S. L., Patton D. R., Simard L., McConnachie A. W., 2008, ApJ, 672, L107
Erb D. K., Shapley A. E., Pettini M., Steidel C. C., Reddy N. A., Adelberger K. L., 2006, ApJ, 644, 813
Freyer T., Hensler G., Yorke H. W., 2006, ApJ, 638, 262
Garnett D. R., 2002, ApJ, 581, 1019
Guedes J., Callegari S., Madau P., Mayer L., 2011, ApJ, 742, 76
Guo Q., White S., Li C., Boylan-Kolchin M., 2010, MNRAS, 404, 1111
Guo K., Zheng X. Z., Fu H., 2013, ApJ, 778, 23
Hao C.-N., Kennicutt R. C., Johnson B. D., Calzetti D., Dale D. A., Moustakas J., 2011, ApJ, 741, 124
Henry A., Martin C. L., Finlator K., Dressler A., 2013a, ApJ, 769, 148
Henry A. et al., 2013b, ApJ, 776, L27
Hirschmann M. et al., 2013, MNRAS, 436, 2929
Kannan R., Stinson G. S., Macciò A. V., Brook C., Weinmann S. M., Wadsley J., Couchman H. M. P., 2014, MNRAS, 437, 3529
Karim A. et al., 2011, ApJ, 730, 61
Katz N., 1992, ApJ, 391, 502
Katz N., Weinberg D. H., Hernquist L., 1996, ApJS, 105, 19
Kauffmann G., 2014, preprint (arXiv:1401.8091)
Kay S. T., Pearce F. R., Frenk C. S., Jenkins A., 2002, MNRAS, 330, 113
Kennicutt R. C., Evans N. J., 2012, ARA&A, 50, 531
Kewley L. J., Ellison S. L., 2008, ApJ, 681, 1183
Lara-López M. A. et al., 2010, A&A, 521, L53
Lara-López M. A. et al., 2013, MNRAS, 434, 451
Lequeux J., Peimbert M., Rayo J. F., Serrano A., Torres-Peimbert S., 1979, A&A, 80, 155
Lilly S. J., Carollo C. M., Pipino A., Renzini A., Peng Y., 2013, ApJ, 772, 119
McCarthy I. G., Schaye J., Font A. S., Theuns T., Frenk C. S., Crain R. A., Dalla Vecchia C., 2012, MNRAS, 427, 379
Maiolino R. et al., 2008, A&A, 488, 463
Mannucci F., Cresci G., Maiolino R., Marconi A., Gnerucci A., 2010, MNRAS, 408, 2115
Marinacci F., Pakmor R., Springel V., 2014, MNRAS, 437, 1750
Moster B. P., Somerville R. S., Maulbetsch C., van den Bosch F. C., Macciò A. V., Naab T., Oser L., 2010, ApJ, 710, 903
Moster B. P., Naab T., White S. D. M., 2013, MNRAS, 428, 3121
Munshi F. et al., 2013, ApJ, 766, 56
Navarro J. F., Steinmetz M., 2000, ApJ, 538, 477
Noeske K. G. et al., 2007, ApJ, 660, L43
Nomoto K., Hashimoto M., Tsujimoto T., Thielemann F.-K., Kishimoto N., Kubo Y., Nakasato N., 1997, Nucl. Phys. A, 616, 79
Pérez-Montero E. et al., 2009, A&A, 495, 73
Piontek F., Steinmetz M., 2011, MNRAS, 410, 2625
Richard J., Jones T., Ellis R., Stark D. P., Livermore R., Swinbank M., 2011, MNRAS, 413, 643
Sáiz A., Domínguez-Tenreiro R., Tissera P. B., Courteau S., 2001, MNRAS, 325, 119
Salmi F., Daddi E., Elbaz D., Sargent M. T., Dickinson M., Renzini A., Bethermin M., Le Borgne D., 2012, ApJ, 754, L14
Shen S., Wadsley J., Stinson G., 2010, MNRAS, 407, 1581
Steinmetz M., Mueller E., 1994, A&A, 281, L97
Stinson G., Seth A., Katz N., Wadsley J., Governato F., Quinn T., 2006, MNRAS, 373, 1074
Stinson G. S., Dalcanton J. J., Quinn T., Kaufmann T., Wadsley J., 2007, ApJ, 667, 170
Stinson G. S., Bailin J., Couchman H., Wadsley J., Shen S., Nickerson S., Brook C., Quinn T., 2010, MNRAS, 408, 812
Stinson G. S., Brook C., Macciò A. V., Wadsley J., Quinn T. R., Couchman H. M. P., 2013, MNRAS, 428, 129
Tremonti C. A. et al., 2004, ApJ, 613, 898
Wada K., Norman C. A., 2007, ApJ, 660, 276
Wadsley J. W., Stadel J., Quinn T., 2004, New Astron., 9, 137
Whitaker K. E., van Dokkum P. G., Brammer G., Franx M., 2012, ApJ, 754, L29
Woosley S. E., Weaver T. A., 1995, ApJS, 101, 181
Wuyts S., Labbé I., Schreiber N. M. F., Franx M., Rudnick G., Brammer G. B., van Dokkum P. G., 2008, ApJ, 682, 985
Wuyts S. et al., 2011, ApJ, 742, 96
Wuyts E., Rigby J. R., Sharon K., Gladders M. D., 2012, ApJ, 755, 73
Zahid H. J., Kewley L. J., Bresolin F., 2011, ApJ, 730, 137
Zahid H. J., Dima G. I., Kewley L. J., Erb D. K., Davé R., 2012, ApJ, 757, 54

This paper has been typeset from a TEX/LATEX file prepared by the author.